The Astrophysical Journal, 870:130 (15pp), 2019 January 10 https://doi.org/10.3847/1538-4357/aaf38a

Millimeter Mapping at $z \sim 1$: Dust-obscured Bulge Building and Disk Growth

Erica J. Nelson[1,2], Ken-ichi Tadaki[3], Linda J. Tacconi[1], Dieter Lutz[1], Natascha M. Förster Schreiber[1], Anna Cibinel[4], Stijn Wuyts[5], Philipp Lang[6], Joel Leja[2], Mireia Montes[7,8], Pascal A. Oesch[9], Sirio Belli[1], Rebecca L. Davies[1], Richard I. Davies[1], Reinhard Genzel[1], Magdalena Lippa[1], Sedona H. Price[1], Hannah Übler[1], and Emily Wisnioski[10]

[1] Max-Planck-Institut für extraterrestrische Physik, Giessenbachstrasse, D-85748 Garching, Germany
[2] Harvard-Smithsonian Center for Astrophysics, 60 Garden St, Cambridge, MA 02138, USA
[3] National Astronomical Observatory of Japan, 2-21-1 Osawa, Mitaka, Tokyo 181-8588, Japan
[4] Astronomy Centre, Department of Physics and Astronomy, University of Sussex, Brighton, BN1 9QH, UK
[5] Department of Physics, University of Bath, Claverton Down, Bath, BA2 7AY, UK
[6] Max Planck Institute for Astronomy (MPIA), Kn¨igstuhl 17, D-69117, Heidelberg, Germany
[7] School of Physics, University of New South Wales, Sydney, NSW 2052, Australia
[8] Astronomy Department, Yale University, New Haven, CT 06511, USA
[9] Observatoire de Genève, 51 Ch. des Maillettes, 1290 Versoix, Switzerland
[10] Research School of Astronomy & Astrophysics, Australian National University, Canberra, ACT-2611, Australia

Received 2017 December 29; revised 2018 November 19; accepted 2018 November 20; published 2019 January 16

Abstract

A randomly chosen star in today's universe is most likely to live in a galaxy with stellar mass between the Milky Way and Andromeda. It remains uncertain, however, how the structural evolution of these bulge-disk systems proceeded. Most of the unobscured star formation we observe by building Andromeda progenitor s at $0.7 < z < 1.5$ occurs in disks, but $\gtrsim$90% of their star formation is reprocessed by dust and remains unaccounted for. Here we map rest-500 μm dust continuum emission in an Andromeda progenitor at $z = 1.25$ to probe where it is growing through dust-obscured star formation. Combining resolved dust measurements from the NOthern Extended Millimeter Array interferometer with *Hubble Space Telescope* Hα maps and multicolor imaging (including new data from the *Hubble* Deep UV Legacy Survey, HDUV), we find a bulge growing by dust-obscured star formation: while the unobscured star formation is centrally suppressed, the dust continuum is centrally concentrated, filling the ring-like structure that is evident in the Hα and UV emission. Reflecting this, the dust emission is more compact than the optical/UV tracers of star formation with $r_e(\text{dust}) = 3.4$ kpc, $r_e(\text{H}\alpha)/r_e(\text{dust}) = 1.4$, and $r_e(\text{UV})/r_e(\text{dust}) = 1.8$. Crucially, however, the bulge and disk of this galaxy are building simultaneously; although the dust emission is more compact than the rest-optical emission ($r_e(\text{optical})/r_e(\text{dust}) = 1.4$), it is somewhat less compact than the stellar mass ($r_e(M_*)/r_e(dust) = 0.9$). Taking the rest-500 μm emission as a tracer, the expected structural evolution can be accounted for by star formation: it will grow in size by $\Delta r_e/\Delta M_* \sim 0.3$ and in central surface density by $\Delta\Sigma_{\text{cen}}/\Delta M_* \sim 0.9$. Finally, our observations are consistent with a picture in which merging and disk instabilities drive gas to the center of galaxies, boosting global star formation rates above the main sequence and building bulges.

Key words: galaxies: bulges – galaxies: evolution – galaxies: star formation – galaxies: structure – galaxies: ISM

1. Introduction

Owing to significant investments in optical and near-infrared instrumentation, we now have high-resolution mapping of large numbers galaxies in the rest-UV+optical in the epoch when they formed most of their stars ($1 < z < 3$). This mapping has shown that most star formation as traced by Hα and UV emission occurs in clumpy, rotating galactic disks (e.g., Förster Schreiber et al. 2006, 2009; Genzel et al. 2006, 2008; Wisnioski et al. 2011, 2015; Kassin et al. 2012; Nelson et al. 2013; Wuyts et al. 2013; Stott et al. 2016). Additionally, studies that map where galaxies are growing via rest-UV/optical tracers of the specific star formation rate (sSFR = SFR/M_*), which trace current star formation relative to the integral of past star formation (e.g., EW(Hα), UV-optical color gradients), typically find either a flat or somewhat centrally depressed sSFR, which means that galaxies generally grow somewhere between self-similarly and inside-out; they do not, on average, become more compact (Nelson et al. 2012, 2013, 2016b; Wuyts et al. 2012; Liu et al. 2016, 2017). However, a significant fraction of star formation is attenuated by dust and may be missed by these types of observations. Most importantly, this hampers our ability to determine where within galaxies most of the stars were formed, and consequently, how galaxies grew through star formation.

Recent studies of the spatially resolved Balmer decrements, colors, and spectral energy distributions (SEDs) of large samples of galaxies have found that with increasing stellar mass, both the normalization and gradient in dust attenuation increases (e.g., Wuyts et al. 2012; Liu et al. 2016, 2017; Nelson et al. 2016a; Wang et al. 2017). At a most basic level, this suggests that the dust-obscured star formation may be distributed differently than the unobscured star formation in massive galaxies. In particular, it may be more compact. In massive galaxies near the peak of the cosmic star formation history ($M_* \gtrsim 2 \times 10^{10}\,M_\odot$ at $z \sim$ 1–2), typically $\gtrsim$90% of the emission from star formation is absorbed by dust and reradiated in the infrared (e.g., Reddy et al. 2006, 2010, 2017; Wuyts et al. 2011; Whitaker et al. 2012, 2014). Thus, to determine how galaxies are building, it is essential to be able to map not only the unobscured star formation but also the obscured star formation. This has been difficult because telescopes operating at the far-IR (FIR) wavelengths that are necessary to probe the peak of the dust emission have had insufficient sensitivity and spatial resolution to map galaxies at $z \sim 1$–3.

With the increased sensitivity and spatial resolution of millimeter/submillimeter (mm/submm) interferometers such as NOthern Extended Millimeter Array (NOEMA) and ALMA, we can now map the dust continuum emission at longer wavelengths, however. For galaxies near the peak of the cosmic SFH at $1 < z < 3$, these interferometers can be used to efficiently probe dust continuum emission at rest-wavelengths $\sim$200–500 μm. For galaxies with high specific star formation rates, FIR-submm emission represents thermal emission from dust that is largely heated by star formation and thus has been used as tracer of obscured star formation (modulo dust temperature gradients; e.g., Barro et al. 2016; Tadaki et al. 2017; although see Section 2.5 for further discussion). A number of individual galaxies have now been mapped at mm and submm wavelengths, revealing in a significant fraction very centrally concentrated molecular gas and dust (e.g., Tacconi et al. 2008, 2010; Ikarashi et al. 2015; Simpson et al. 2015, 2017; Barro et al. 2016; Hodge et al. 2016; Tadaki et al. 2017). Very compact sizes have also been found in bright sources at centimeter wavelengths (10GHz; Murphy et al. 2017). In these massive galaxies, while star formation as traced by Hα emission is in extended rotating disks, the star formation inferred from dust emission is much more centrally concentrated, which builds their centers (Genzel et al. 2013; Tadaki et al. 2017). This suggests that dust-obscured in situ star formation could be an important formation channel for the dense cores of massive galaxies. With $M_* \sim 10^{11}\,M_\odot$ at $z \sim 2$, these galaxies are likely to be the progenitors of today's massive elliptical galaxies. The next key question is how dust-obscured star formation is distributed in the progenitors of today's M* galaxies at the equivalent epoch, pushing dust mapping from the most massive galaxies down to more typical galaxies.

It remains uncertain which processes are responsible for building bulges in local massive spirals (e.g., Kormendy 2016). Even for the closest, best-studied examples of the Milky Way and Andromeda, the fossil record (stellar ages, abundances, dynamics, and structural parameters) points to a first rapid and dissipative formation event followed by secular growth, but the mechanisms involved remain unclear (e.g., Saglia et al. 2010; Courteau et al. 2011; Dorman et al. 2012; Bland-Hawthorn & Gerhard 2016). In recent years, theoretical considerations, numerical simulations, and empirical results on the structure and kinematics of high-z star-forming galaxies have brought forward new bulge formation channels through efficient disk-internal dissipative processes in the typically gas-rich and turbulent $z \sim 2$ disks. These $z \sim 2$ disks typically have baryonic gas mass fractions of $\sim$30%–50% (e.g., Tacconi et al. 2013) and intrinsic gas velocity dispersions $\sim$25–50 km s^{-1} (Förster Schreiber et al. 2006, 2009; Genzel et al. 2006; Kassin et al. 2007; Epinat et al. 2009; Law et al. 2009; Newman et al. 2013; Wisnioski et al. 2015; Stott et al. 2016). In these gas-rich turbulent disks, processes like violent disk instabilities and inward migration of giant star-forming clumps may even lead to "classical" bulges without the need for merger events (e.g., Immeli et al. 2004; Genzel et al. 2008; Dekel et al. 2009; Zolotov et al. 2015; Bournaud 2016), although the importance of these processes is debated (e.g., van Dokkum et al. 2015; Lilly & Carollo 2016). With evolving gas inflow rates, sizes, merger rates, and surface densities of gas and stars, the physics of disks at $z \sim 1$ may be very different. In particular, is this how the bulges of M* galaxies in the local universe are built? Do they have an equivalent central dust-obscured star formation phase before quenching? The potentially complex bulge formation histories underscore the importance of in situ studies at epochs when galaxies were most actively forming their stars.

Based on abundance-matching arguments, we can link progenitor-descendant populations across cosmic time (e.g., Conroy & Wechsler 2009; Behroozi et al. 2013; Leja et al. 2013; Moster et al. 2013; van Dokkum et al. 2013; Papovich et al. 2015; Torrey et al. 2015, 2017; Wellons & Torrey 2017). In this paper we use abundance matching to select a galaxy that based on its stellar mass is likely to have the same mass as Andromeda at $z = 0$. Throughout this paper, when we refer to this galaxy as an Andromeda progenitor, we mean that it is likely to be the progenitor of a galaxy that is part of the population of galaxies at $z = 0$ that have the same mass as Andromeda. The evolution of this population of galaxies inferred from abundance matching is shown in Figure 1. Andromeda has a stellar mass of $M_* = 1$–$1.5 \times 10^{11}\,M_\odot$, $\sim$30% of which is in the bulge (e.g., Geehan et al. 2006; Tamm et al. 2012). $z \sim 1$ is a crucial epoch for studying bulge growth in these galaxies, with steadily increasing Sérsic indices suggesting significant structural evolution and bulge build-up (e.g van Dokkum et al. 2013; Lang et al. 2014; Papovich et al. 2015). Probably related, the quenched fraction also increases during this epoch, with the quiescent fraction among Andromeda progenitor increasing from 47% at $z = 1.4$ to 70% at $z = 0.7$ (Papovich et al. 2015).

In this paper, we combine new spatially resolved 1.1mm (rest-500 μm) data with *Hubble Space Telescope* Hα maps and UV-NIR imaging to investigate growth patterns in the progenitor of an Andromeda progenitor galaxy at $z = 1.25$. This paper is organized as follows. In Section 2 we describe the target selection, the reduction and analysis of the NOEMA and *HST* data, and the derivation of spatially resolved stellar population properties. In Section 3 we discuss the derivation structural parameters of galaxy growth in rest-500 μm, Hα, UV, rest-optical continuum, and stellar mass. We compare the size, concentration, and radial profiles (SFR and sSFR) in the different tracers as well as the effectiveness of an SED-based dust correction to the Hα and UV data. In Section 4 we consider structural growth due to star formation in the context of the evolution of central density via the Σ_1–M_* relation and the expected size evolution of Andromeda progenitors. Additionally, we compare the dust continuum size of our Andromeda progenitor to sizes measured for the progenitors of massive elliptical galaxies from Tadaki et al. (2017).

2. Data

2.1. Selection

The aim of this initiative was to map the submm dust continuum emission in the progenitor of an M* galaxy during the time when it was likely to be building its bulge around $z \sim 1$. Additionally, the availability of Hα maps at *HST* resolution for galaxies with $0.7 < z < 1.5$ allows for a direct comparison between the distribution of obscured and unobscured tracers of star formation. We selected galaxies with stellar masses between the expected stellar masses of Milky

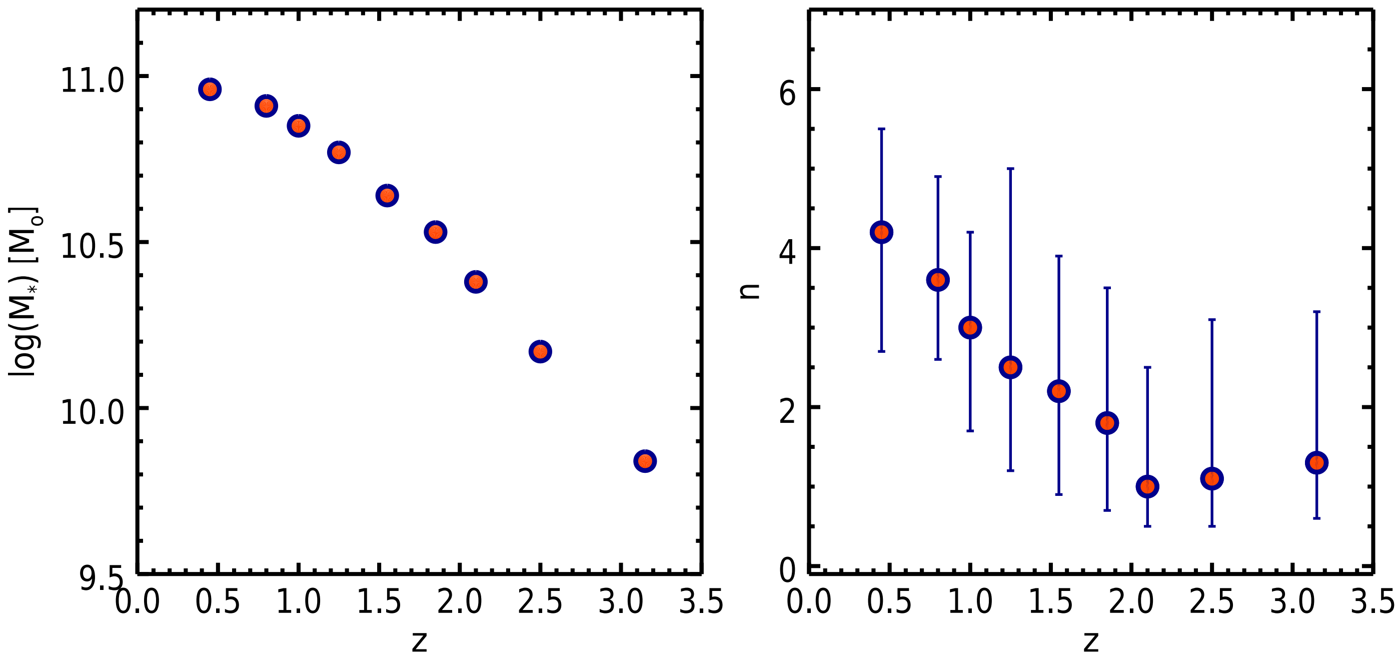

Figure 1. Left: Average stellar mass evolution of galaxies with a present-day mass of Andromeda based on abundance matching (Behroozi et al. 2013; Moster et al. 2013). In this paper we select a galaxy that based on its stellar mass is likely to be a $z \sim 1$ progenitor of a galaxy with present-day mass similar to the mass of Andromeda (Papovich et al. 2015). Right: Evolution of the H_{F160W} Sérsic indices with time (Papovich et al. 2015). The steady increase in Sérsic indices during the epoch of this study suggests that this is a critical epoch for understanding the growth of galactic bulges.

Way and Andromeda progenitors in this redshift range based on abundance matching (Moster et al. 2013; see Figure 1). To facilitate our exploratory study with NOEMA, we wished to target a galaxy for which we have a sufficiently high signal-to-noise ratio (S/N) to accurately measure the radial distribution and effective radius of the Hα emission for comparison to the rest-500 μm data. Finally, we required galaxies to have high SFR(IR) $> 50\,M_{\odot}$ yr^{-1} based on *Spitzer*/MIPS and *Herschel*/PACS plus $r_e > 0\farcs5$ to optimize detection and spatially resolved mapping with NOEMA. Two galaxies were observed with NOEMA for relatively short integrations at a lower resolution than the one with the stronger detection that was chosen for mapping. Thus, the pilot target selected for this exploratory study was GOODSN-18574 (ID from 3D-*HST* v4.1 catalog) with coordinates (12:37:02.739, 62:14:01.663) This galaxy has a redshift z = 1.248, a stellar mass $M_* = 6.76 \times 10^{10}\,M_{\odot}$ (Skelton et al. 2014; Momcheva et al. 2016), a star formation rate[11] SFR (IR, Hα, UV) = (164,28,5) $M_{\odot}$ yr^{-1} (Whitaker et al. 2014; Momcheva et al. 2016), and an effective radius $r_e(H_{F160W}) = 0\farcs56$ (van der Wel et al. 2012). The derivation of these properties is described in more detail in Sections 2.3 and 2.5. This galaxy is roughly on the size-mass relation (van der Wel et al. 2014) and ~0.55 dex above the SFR-mass relation at this redshift (Whitaker et al. 2014). If the current star formation rate were to remain constant, this galaxy would exceed the mass of Andromeda by $z = 1.0$. However, in a framework in which galaxies oscillate above and below the main sequence as a result of changes in accretion rate, this galaxy is likely experiencing a short excursion above the main sequence before its star formation is regulated back to a rate typical of its stellar mass (e.g., Forbes et al. 2012, 2014; Nelson et al. 2016b; Tacchella et al. 2016a, 2016b, 2018; Orr et al. 2017; Sparre et al. 2017).

[11] These Hα and UV SFRs are not dust-corrected.

2.2. NOEMA Data Reduction and Analysis

Dust continuum observations were taken with the IRAM NOEMA between 2016 December and 2017 March. We observed our primary target, GOODSN-18574, for a total on-source integration time of 26 hr in three configurations of the eight antennas: 9hr in D, 3hr in C, and 14hr in A (in order from most compact to most extended configuration). Data were taken with the antennas arranged into multiple configurations to efficiently probe emission on multiple scales. We used the compact C and D configurations to probe faint, extended emission (e.g., from a galaxy disk) and the extended A configuration to probe bright, compact emission (e.g., from a galaxy bulge). Observations were carried out in band 3 at 265 GHz (1.1 mm), allowing us to measure the rest-500 μm dust continuum emission for our target at $z = 1.248$. Although this tuning approached the high-frequency/short wavelength limit of NOEMA's range where atmospheric transmission is lower, this is compensated for by the increasing brightness of the source moving up the Raleigh-Jeans tail. The conditions varied but were excellent during observations in A configuration. The primary source of atmospheric opacity, the percipitable water vapor (PWV), was low for the A configuration tracks, PWV < 1 mm, which is particularly important for these observations that are at the high-frequency extrema of NOEMA's range. The noise in the system as reflected in the system temperature was $T_{\rm sys} < 200$. For data taken in the C and D configurations, these values were PWV = 3–4 mm and $200 < T_{\rm sys} < 400$. Observations of the source were alternated with observations of a bright quasar every 20 minutes as a calibrator. The WideX correlator with a bandwidth of 3.6 GHz was used for maximum continuum sensitivity.

The data were calibrated following the standard GILDAS/CLIC pipeline performing absolute flux, bandpass, phase, and amplitude calibrations. Additional flagging was done by hand. We combine the amplitudes and *uv* distances that comprise the

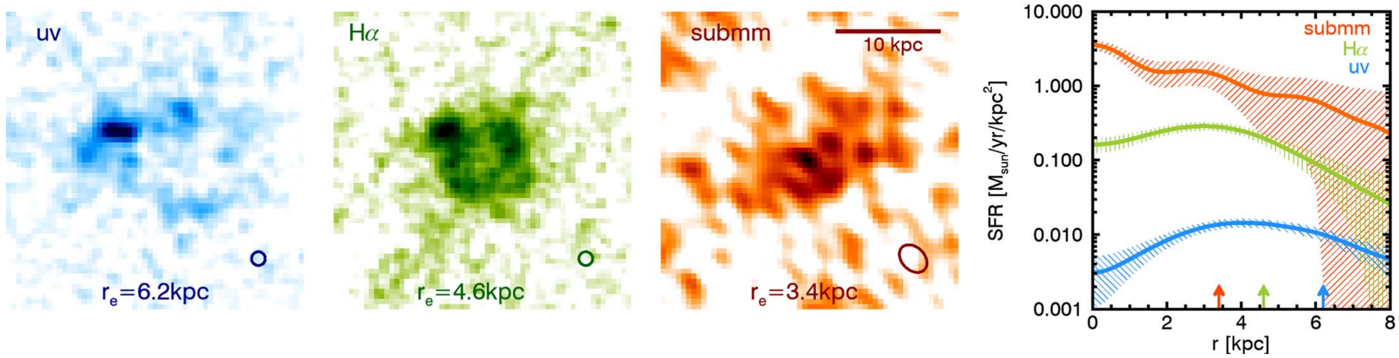

Figure 2. Images and surface brightness profiles of the star formation in GOODSN-18574 as traced by rest-UV, Hα from *HST*, and rest-submm (rest-500 μm) from NOEMA. The effective radius in each band is listed at the bottom of the image and shown as an arrow in the plot of the radial profiles. It is clear from the images, surface brightness profiles, and radii that the different tracers of star formation trace very different regions. The star formation becomes more compact moving from less to more obscured tracers. The UV is only seen at large radii, the Hα is somewhat more compact, but still centrally depressed, while the submm region is centrally concentrated. The Hα and even more so the UV exhibit ring-like structures that are filled in by the dust-obscured star formation as traced by the submm emission. The dark circles and ellipses in the bottom right corner show the FWHM resolution of the images. The shaded regions reflect the uncertainties due to the noise in the images.

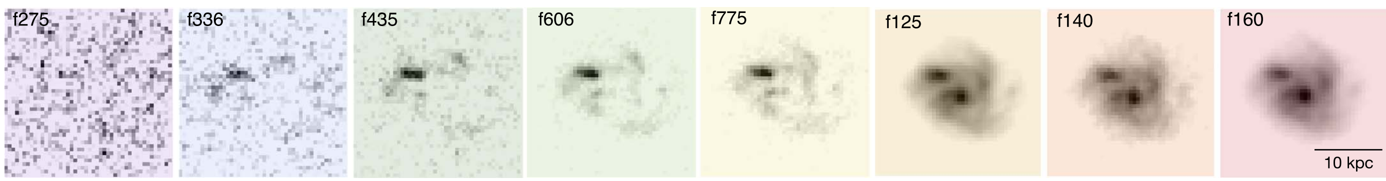

Figure 3. *U* - *H* band imaging with *HST*. This galaxy exhibits strong color gradients. At bluer wave bands, the emission is increasingly suppressed in the center.

visibility data for all configurations of the antennas into a single data set and use GILDAS/MAPPING to Fourier-transform the combined data from *uv* space to image space. We use "Robust" weighting with a robust weighting threshold of 2.3 to give increased weight to long-baseline data. This image has a beam size of $0.28'' \times 0.39''$ and rms noise of 32 μJy/beam. We use a single clean iteration to correct the absolute flux scale of the image, but further deconvolution is not warranted by the S/N of our data. Instead, when necessary, we convolve our comparison data sets to the resolution of the NOEMA data. The dust continuum image is shown in Figure 2.[12]

2.3. Ancillary Data: Hubble Imaging and Spectroscopy, and Spitzer and Herschel Photometry

We leverage our NOEMA data using a wealth of ancillary data that thanks to large investments by the community have been obtained and publicly released. These data include spatially-resolved imaging from *HST* in eight bands spanning UV through near-infrared wavelengths, as shown in Figure 3. The rest-UV is probed by F275W, F336W (HDUV, Oesch et al., submitted), F435W, F606W, and F775W (GOODS Giavalisco et al. 2004). The rest-optical is probed by F125W, F160W (CANDELS Grogin et al. 2011; Koekemoer et al. 2011), and F140W (Skelton et al. 2014, 3D-*HST*). We use the mosaics provided by the 3D-*HST*[13] and HDUV[14] teams (Skelton et al. 2014, Oesch et al. 2018). The rest-IR is probed by Spitzer/IRAC 3.6 μm, 4.5 μm (Ashby et al. 2013); 5.8 μm, 8 μm (Dickinson et al. 2003; Ashby et al. 2013); and *Herschel*/PACS 70 μm,100 μm, 160 μm (PEP Lutz et al. 2011) We note that these rest-IR tracers are not spatially resolved for galaxies at $z \sim 1$.

The redshift of GOODSN-18574 was derived based on combined constraints from photometry and 3D-*HST* spectroscopy (Brammer et al. 2012; Momcheva et al. 2016). A stellar mass of $6.8 \times 10^{10}\, M_\odot$ was computed by fitting a stellar population synthesis model to the observed U-8 μm photometry, using Bruzual & Charlot (2003) templates and assuming solar metallicity, a Chabrier (2003) initial mass function, an exponentially declining star formation history, and the Calzetti et al. (2000) dust attenuation law (see Skelton et al. 2014).

We make an Hα map of this galaxy using data from the 3D-*HST* grism spectroscopic survey (van Dokkum et al. 2011; Brammer et al. 2012; Momcheva et al. 2016). To make the Hα map of GOODSN-18574, we subtract quantitative models for both the contamination from overlapping spectra of other objects and stellar continuum emission. The continuum model is generated by convolving the best-fit SED with the combined $J_{F125W}/JH_{F140W}/H_{F160W}$ image and accounts for a spatially resolved stellar absorption. With a FWHM spectral resolution of ∼100 Å, Hα λ6563Å and [N II] λλ6548+6583 Å are blended. To account for the contamination of Hα by [N II], we assume flat radial gradients, scale the measured flux down by a factor of $\mathrm{H}\alpha_{\mathrm{corr}} = \mathrm{H}\alpha_{\mathrm{meas}}/1.3$, and adopt $\mathrm{H}\alpha_{\mathrm{corr}}$ as the Hα flux (Wuyts et al. 2014, 2016). For a more detailed description, see Nelson et al. (2016b).

2.4. Spatially Resolved Stellar Population Properties

Spatially resolved maps of stellar mass and dust attenuation made from the eight-band *HST* imaging are shown in Figure 4. The creation of these maps is covered in detail in Cibinel et al. (2015), but we briefly describe it here for completeness. Image

[12] As a potentially helpful side note: following the imaging procedure, the interferometric images are in units of Jy/beam. To ensure that the flux scale is independent of beam size requires scaling by the beam solid angle for an elliptical Gaussian with half-power beam width major and minor axes *a* and *b* $\pi ab/(4\ln 2)$.

[13] http://3dhst.research.yale.edu/Data.php

[14] http://www.astro.yale.edu/hduv/data.html

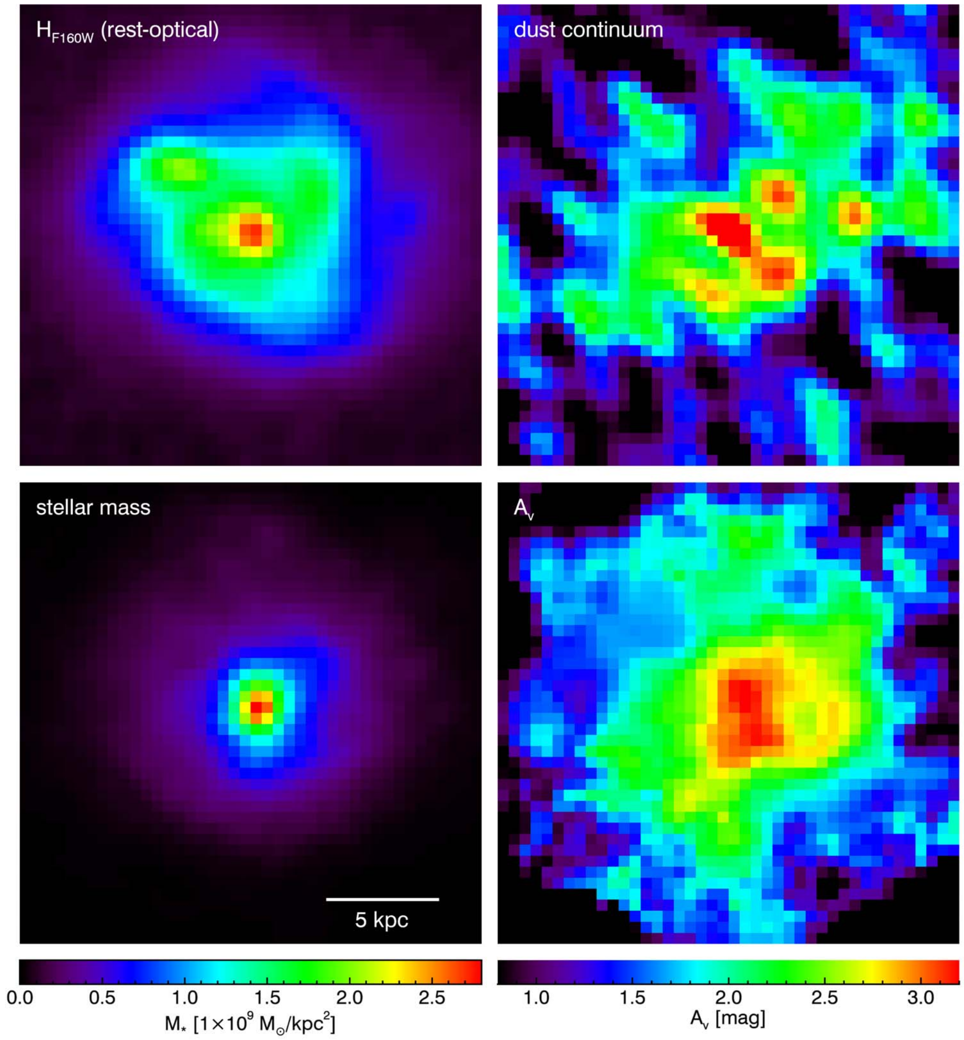

Figure 4. Top row: Observed quantities. The *HST* H_{F160W} and NOEMA dust continuum images. Bottom row: Maps derived from spatially resolved stellar population synthesis modeling. Maps of stellar mass and dust reddening.

postage stamps are cut from the mosaics in each *HST* band (Figure 3). The images in different bands clearly show that this galaxy exhibits strong color gradients: redder in the center and bluer at larger radii. The reddening can be due to age, dust, or both, and it will affect inferences about the distribution of star formation and stellar mass. Rest-UV colors can be used to help distinguish between the effects of dust and age (see, e.g., Liu et al. 2017). Postage stamps are convolved by matching the point-spread function (PSF) to the resolution of the reddest band (H_{F160W}, which has the lowest resolution). These images are then adaptively smoothed using Adaptsmooth (Zibetti et al. 2009), which requires an $S/N > 5$ in each spatial bin in the H_{F160W} image. This image has the highest S/N. A potential cause for concern is that this may result in an additional smoothing in the galaxy center where the surface brightness changes most rapidly. This concern is alleviated, however, by noting that the center is bright and has a high S/N in H_{F160W}, so that no smoothing is done inside 6 kpc, which is significantly larger than the H_{F160W} effective radius of 4.7 kpc. The SPS code LePhare (Arnouts et al. 1999; Ilbert et al. 2006) is run on the photometry in each spatial bin using the Bruzual & Charlot 2003 synthetic spectral library, a Chabrier (2003) initial mass function (IMF), a Calzetti et al. (2000) dust law, and three metallicity values ($Z = 0.2, 0.4, 1\, Z_{\odot}$). We adopt a delayed exponential star formation history $(t/\tau^2)\exp(-t/\tau)$ with a characteristic timescale τ with 22 values between 0.01 and 10 Gyr and a minimum age of 100 Myr. This method is qualitatively similar to that described in Wuyts et al. (2012) and Lang et al. (2014). Despite using slightly different assumptions and different SPS codes, within 8 kpc ($1.7 r_e$), the stellar mass maps from these two methods are typically the same to within 20%.

2.5. Star Formation Indicators

Figure 2 shows the three different tracers of star formation we have for GOODSN-18574: UV, Hα, and submm. First, the rest-UV (1216–3000 Å) traces emission from stars with lifetimes <100 Myr, and the following can be used to scale the UV luminosity to a star formation rate on this timescale. We adopt the conversion of Madau & Dickinson (2014) scaled down by a factor of 0.63 to convert from a Salpeter (1955) into a Chabrier (2003) IMF,

$$\mathrm{SFR} = 7.2 \times 10^{-28} L_{\nu}(\mathrm{UV}),$$

where L_{ν}(UV) is the UV luminosity in units of erg^{-1} s^{-1} Hz^{-1}. We probe the rest-UV emission with the HST/B_{F435W} filter, corresponding to a rest-frame 1921 Å, which is near the center of the optimal wavelength range for determining UV-based star formation rates according to Madau & Dickinson (2014).

Second, the Hα recombination line reemits emission shortward of the Lyman limit, providing a probe of stars with lifetimes <10 Myr. To scale the Hα luminosity to a star formation rate, we use the relation presented in Kennicutt (1998) adapted from a Salpeter to a Chabrier (2003) IMF,

$$\mathrm{SFR(H}\alpha) = 1.7 \times 10^{-8} L_{\mathrm{H}\alpha}[L_{\odot}].$$

With a rest wavelength of 6563 Å, Hα is less impacted by dust attenuation than the UV, but it still is significantly attenuated in dusty galaxies.

Third, the bulk of the bolometric luminosity from young massive stars is absorbed and reradiated in the IR, with a peak in emission near 100 μm (e.g., Lutz et al. 2016). The total infrared luminosity is computed from *Herschel*/PACS 160 μm (Lutz et al. 2011; Magnelli et al. 2013) using a luminosity-independent template (Wuyts et al. 2011) and scaled to a star formation rate using

$$\mathrm{SFR(IR)} = 1.09 \times 10^{-10} L_{IR}[L_{\odot}].$$

In intermediate- and high-redshift galaxies, this FIR emission is not resolved with *Herschel*. The only currently feasible way to resolve long-wavelength dust emission in intermediate- and high-redshift galaxies is using mm/submm interferometers. Here we take advantage of the high resolution and continuum sensitivity of the NOEMA millimeter interferometer to remap the rest-500 μm dust continuum emission. We scale this rest-500 μm image to the total SFR(IR) computed from the *Herschel*/PACS 160 μm and use it as a proxy for dust-obscured star formation.

Before moving on to our findings, we would like to discuss a few caveats. First, the source of the dust heating that powers the rest-FIR to submm emission remains debated. In the local universe, old stars can contribute significantly to the heating of dust (e.g., Lonsdale Persson & Helou 1987; Walterbos & Greenawalt 1996; Montalto et al. 2009; Bendo et al. 2010, 2012, 2015; Smith et al. 2012), but in the more rapidly star-forming galaxies of the higher redshift universe, dust heating is likely dominated by young stars (e.g., Barger et al. 1998; Blain et al. 2002; Coppin et al. 2008; Pope et al. 2008; Menéndez-Delmestre et al. 2009; Hayward et al. 2011; Hodge et al. 2012; Simpson et al. 2015; Ikarashi et al. 2015). If old stars contribute significantly to the heating of the dust, the presence of a bulge in this galaxy might cause the intrinsic dust-obscured star formation to be less centrally concentrated than we infer. At 170 $M_{\odot}$ yr^{-1}, the star formation rate of this galaxy is only $\sim$2–5$\times$ lower than a typical submm galaxy (SMG) and $\gtrsim$50$\times$ higher than a local spiral. Given the strong dependence of dominant heating source on specific star formation rate and the high sSFR of 2.5×10^{-9} yr^{-1} of this galaxy, no more than $\sim$10% of the IR emission in this galaxy is likely to be due to old stars (Leja et al. 2018). This estimate is based on forward-modeling the observed UV-IR photometry with a physical model that includes a complex star formation history and flexible dust attenuation model using the PROSPECTOR inference framework (Leja et al. 2017). As a test, we compute what the expected rest-500 μm flux is based on by extrapolating from fluxes at shorter wavelengths near the peak of the dust emission. If a significant fraction of the rest-500 μm emission is due to heating by old stars, and if old stars account for a larger fraction of the heating at rest-500 μm than at $\lambda < 160$ μm, then the measured rest-500 μm flux should exceed the flux that is predicted based on extrapolating the flux from shorter wavelengths. We compute the expected rest-500 μm flux using a modified blackbody with temperatures $T = 25$–35 K and graybody spectral indices $\alpha = 1$–2 (shown in Figure 5). Expected rest-500 μm fluxes based on this extrapolation are $S_{500} = 0.6$–2 mJy, while we measure a rest-500 μm flux of $S_{500} = 0.5 \pm 0.1$ mJy in GOODSN-18574. The measured flux is consistent with or lower than we would expect based on the brightness of this galaxy at $\lambda_{\mathrm{rest}} < 160$ μm, meaning that there is little room for an additional heating source at long wavelengths.

Additionally, the flux at rest-frame wavelengths >200 μm may be a better tracer of dust mass than dust luminosity, suggesting that it may be a better tracer of molecular gas mass than star formation rate (e.g., Scoville et al. 2014). We test the effect on our results of interpreting the rest-500 μm emission as tracer molecular gas mass rather than star formation. Instead of scaling rest-500 μm directly to star formation, we instead use it to infer the dust attenuation. To do this, we first infer the molecular gas mass surface density based on the rest-500 μm surface brightness (Scoville et al. 2016, Equation (16)). From the molecular gas column density, we infer the optical depth (e.g., Genzel et al. 2013). Translating this into an effective screen, we then use the inferred dust attenuation to dust-correct the Hα-based SFR profile. Figure 6 shows a comparison of these two interpretations of the rest-500 μm emission. The upshot is that the radial distributions of star formation inferred using these two different methods are similar, and hence our results are not impacted by this choice.

Finally, our scaling assumes a flat temperature gradient across the galaxy, while local galaxies typically exhibit negative temperature gradients (i.e., hotter temperatures in the center; e.g., Engelbracht et al. 2010; Pohlen et al. 2010; Galametz et al. 2012; Hunt et al. 2015). If this were the case in this galaxy, this effect would cause the intrinsic dust-obscured star formation to be more centrally concentrated than we infer.

3. Structural Properties of Galaxy Growth

Figure 2 shows the images and radial surface brightness profiles of the different tracers of star formation in GOODSN-18574 and Figure 10 shows the three color image. It is immediately clear that the dust-obscured star formation is more concentrated than the unobscured star formation. In this section we quantify the structural properties of growth in GOODSN-18574 using the size, concentration, and radial surface brightness profiles. We compare these quantities among the different star formation tracers UV, Hα, and dust continuum emission and between stellar mass and rest optical light. By comparing the structural parameters of star formation to those of the stellar mass, we infer how this galaxy is growing through star formation.

3.1. Size

We measure the size of the dust continuum emission directly from the visibility data (as shown in Figure 7). The advantage of fitting the observed visibilities directly in the interferometric *uv*-plane rather than in the image plane is that the uncertainties

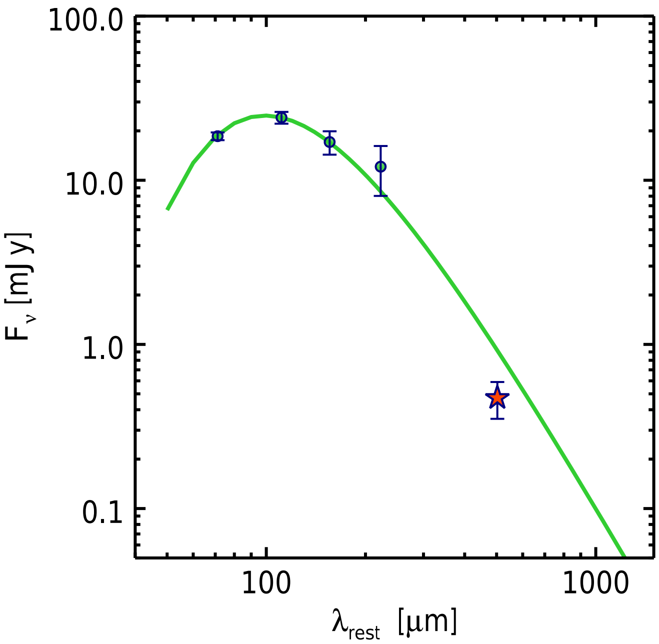

Figure 5. Dust SED. Points show observed FIR-mm photometry for GOODSN-18574: green points are from *Herschel* (Elbaz et al. 2011; Lutz et al. 2011; Magnelli et al. 2013), and the orange star is from NOEMA. The line shows a modified blackbody SED with a graybody spectral index $\alpha = 1.6$ (e.g., Casey 2012) and best-fit temperature $T = 32$ K. The measured rest-500 μm flux from NOEMA is consistent with or lower than we would expect based on the brightness of this galaxy at $\lambda_{\rm rest} < 160$ μm, meaning that there is little room for an additional heating source at long wavelengths. See Section 2.5 for further discussion.

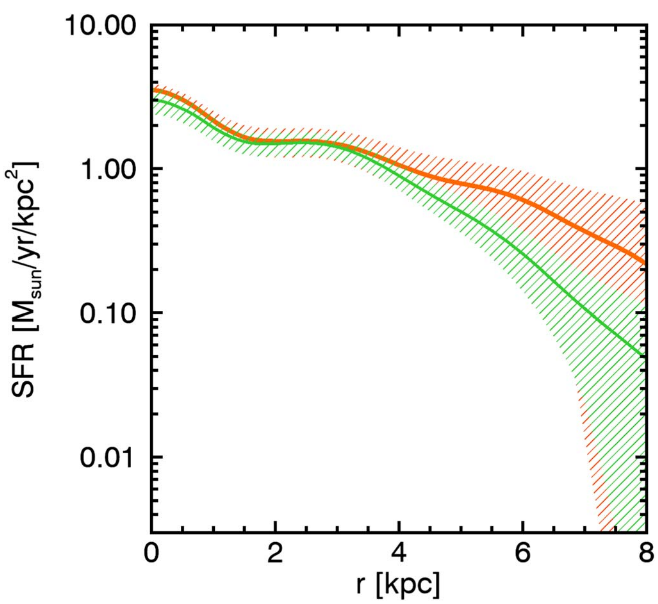

Figure 6. Radial distribution of star formation. Orange shows the radial profile of star formation inferred by scaling the rest-500 μm emission directly to star formation. Green shows the radial profile of star formation inferred by instead interpreting the rest-500 μm emission as a tracer of molecular gas, using the molecular gas column density to infer dust attenuation, and using this map of dust attenuation to correct the Hα-based star formation rate profile for dust. The results of these two methods are very similar. (See Section 2.5).

associated with the complex mathematical transformations performed in the imaging process are removed. Furthermore, choices made to improve the spatial resolution during our imaging procedure do not impact our size measurement (specifically, flux is not resolved out). In this method, each model flux distribution is convolved with the beam in image space, Fourier-transformed to *uv*-space, then resampled to the observed UV baselines. The fitting is performed using a circular Gaussian model with the centroid, flux, and FWHM as free parameters. The best fit is then determined by χ^2 minimization. We find r_e(rest-500 μm) $= 3.4 \pm 0.7$ kpc. We obtain this fit using the GILDAS/mapping routine UVFIT; the results are the same within the errors when CASA/UVMODELFIT is used. If we instead fit with the physically better motivated exponential, we find r_e(rest-500 μm) $= 3.7$ kpc, which is well within the uncertainties of the fit.

We measure sizes for the rest-optical data (specifically JH_{F140W}, which traces the $\lambda_{\rm rest} = 6220$ Å light) and stellar mass map by fitting Sérsic models (Sérsic 1968) convolved with the PSF of the images using GALFIT (Peng et al. 2002). For the mass map, we used the empirical H_{F160W} PSF (the PSF to which all images that contribute to making the mass map are convolved). For the JH_{F140W} image we use the interlaced PSF generated by the code Tiny Tim (Krist 1995). We determine error bars by performing Monte Carlo simulations that force the values of the centroid and Sérsic index to remain fixed. We vary the centroid within a $0\farcs2$ box and the Sérsic index by $\pm 50\%$. Neither the Hα nor UV emission are centrally peaked, so they are poorly fit by Sérsic models, and correcting for the PSF is unimportant for a determination of the size. Instead, we measure their sizes using growth curves. The radial surface brightness profiles are measured in finely sampled circular apertures, and r_e is the radius at which the the enclosed flux is 50% of the total. We determine the uncertainties on the growth curve sizes by taking the standard deviation of Monte Carlo simulations run varying the centroid within a box of $0\farcs2$. We find r_e(optical) $= 4.7 \pm 0.2$ kpc, r_e(mass) $= 2.9 \pm 0.2$ kpc, r_e(UV) $= 6.2 \pm 0.2$ kpc, and r_e(Hα) $= 4.8 \pm 0.2$ kpc,

With regard to star formation tracers, we find r_e(UV) $>$ r_e(Hα) $>$ r_e(submm). That is, the submm, which traces dust-obscured star formation, is the most compact, the UV, which traces unobscured star formation is most extended, and the Hα, which is somewhat less impacted by dust attenuation, is in the middle. Given that the UV size is nearly twice that of the submm size, it is clear that gradients in dust attenuation play a significant role in this galaxy. The true distribution of star formation is more compact than would be inferred based on the Hα or UV emission alone. If GOODSN-18574 had a negative temperature gradient, then the dust-obscured star formation would be even more compact than we measure.

We find that the stellar mass distribution inferred from spatially resolved SED fitting is more compact than the rest-optical light. Comparing the distribution of star formation to existing stellar mass, we find r_e(UV) $>$ r_e(Hα) $\geqslant$ r_e(optical) $>$ r_e(submm) $\geqslant$ r_e(mass). Thus, the extent of the dust emission is similar to or more extended than the stellar mass. Even though the the star formation is more compact than the unobscured tracers suggest, the mass is also more compact than the rest-optical light suggests. This galaxy is still building from the inside out (i.e., growing larger in size due to star formation).

3.2. Concentration

We compute the concentration by dividing the flux in a central aperture by the total flux. As an estimate of concentration, we measure $C = F(r < 0\farcs3)/F(r < 1'')$. This

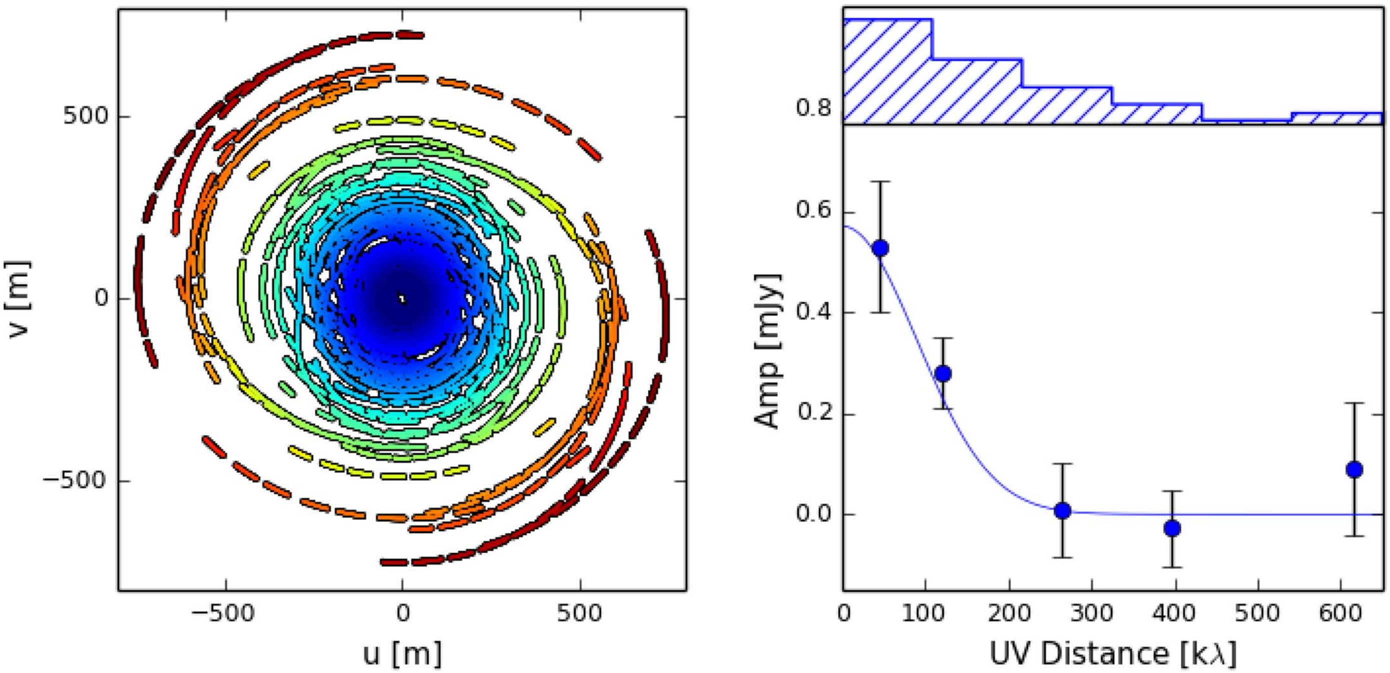

Figure 7. Fit of the size of the rest-500 μm continuum in the *uv* plane. Left: Data as a function of position in the *uv* plane. Right: Data averaged in bins of UV distance, with the fit overplotted as a line. The histogram reflects the quantity of data in each bin of *uv* distance.

number is related to the bulge-to-total ratio in a galaxy (e.g., Abraham et al. 1994, 1996; Lotz et al. 2004). We choose this definition of concentration to optimally use the information content of the new interferometric mm data presented in this paper. From the rest-500 μm image we measure a concentration of $C(\text{rest-500}\,\mu\text{m}) = F(r < 0\farcs3)/F(r < 1'') = 0.24 \pm 0.03$. The uncertainty is determined by taking the standard deviation of Monte Carlo simulations run by varying the centroid within a box of $0\farcs2$. To compare this concentration to the concentration of other star formation tracers as well as to optical emission and stellar mass, we use iraf PSFMATCH to convolve the Hα, UV, and optical images as well as the stellar mass map to the resolution of the NOEMA data. With these PSF-matched images, we then measure concentrations in an identical way. We find $C(\text{H}\alpha) = 0.12 \pm 0.01$, $C(\text{UV}) = 0.04 \pm 0.02$, $C(\text{optical}) = 0.18 \pm 0.01$, and $C(\text{mass}) = 0.33 \pm 0.02$.

Analogously to the trends for effective radius, we find $C(\text{UV}) < C(\text{H}\alpha) < C(\text{optical}) < C(\text{rest-500}\,\mu\text{m}) < C(\text{mass})$. The mm emission is more concentrated than the Hα emission, which in turn is more concentrated than the UV emission. The dust-obscured star formation is more centrally concentrated than the unobscured star formation: the dust-obscured star formation is growing the bulge. The rest-500 μm emission is also more centrally concentrated than the rest-optical emission, but not more so than the stellar mass. Based on comparing the size and concentration of the rest-500 μm emission to the the rest-optical, which is often taken as a proxy for stellar mass, we would infer that the star formation is more compact than the stellar mass, implying that star formation is actually shrinking the effective radius of the galaxy. However, if we instead compare the size and concentration of the rest-500 μm emission to those of the modeled stellar mass map, this is not the case. The bulge of this galaxy is undergoing a period of growth, but this growth is not so dramatic that it makes the galaxy shrink in size.

3.3. Radial Profiles of SFR and sSFR

Finally, we consider the radial SFR profiles in GOODSN-18574 by comparing the obscured and unobscured tracers of star formation (Figure 8). We additionally show where this galaxy is growing by comparing the radial distribution of star formation and stellar mass using the specific star formation rate $\text{sSFR} = \text{SFR}/M_*$ (Figure 9). We extract radial profiles from the images of star formation made as described in Section 2.5 that have been convolved such that their PSFs match the spatial resolution of the NOEMA data. This galaxy is fairly round ($b/a = 0.83$ in H_{F160W}), therefore we extract radial profiles in circular apertures centered on the H_{F160W} flux-weighted centroid (which is also the center of mass).

The radial profiles of star formation are shown in Figure 8 (as well as in Figure 2). The dust-obscured star formation dominates the unobscured star formation at all radii. It is roughly an order of magnitude greater than the Hα-based star formation rates and nearly two orders of magnitude greater than the UV-based star formation rates. It is not just an offset between the three tracers, however: the profiles also have markedly different shapes, reflecting the results from simpler size and concentration measurements. While the Hα, and to an even greater extent the UV, are centrally depressed, the dust is centrally peaked. There is significantly more dust-obscured bulge growth than is implied by the unobscured tracers.

Figure 9 shows the radial profile of the specific star formation rate and the star formation rate per unit stellar mass ($\text{sSFR} = \text{SFR}/M_*$), which is a reflection of the rate of growth relative to the stellar mass already present. This quantity is derived as the quotient of the SFR surface density inferred from the dust continuum emission and the stellar mass map convolved to the same resolution. We also show in Figure 9 the radial Hα equivalent width profile, which effectively is the scaled quotient of the Hα and respective broadband emission, which is often used as a tracer of sSFR. Comparing the radial profiles of EW(Hα) and the dust continuum based sSFR, we

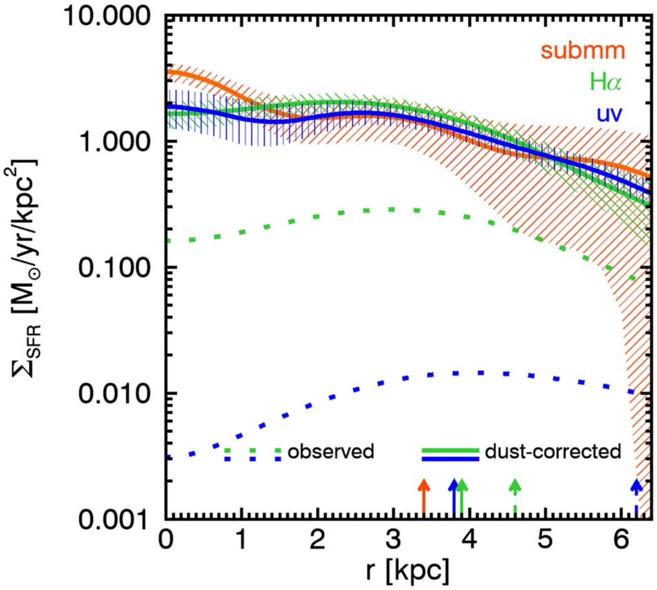

Figure 8. Dashed lines show the radial distribution of star formation inferred from Hα (green) and UV (blue) with no dust correction; the respective solid lines show these profiles corrected for dust attenuation using the rest UV-optical SED (see Section 3.3). The dust-obscured star formation inferred from the rest-500 μm emission is shown in red. After correcting for dust using the SED Av map, the Hα and UV trace the rest-500 μm emission fairly well in a radially averaged sense. There does appear to be some excess central emission, but this is too obscured to recover.

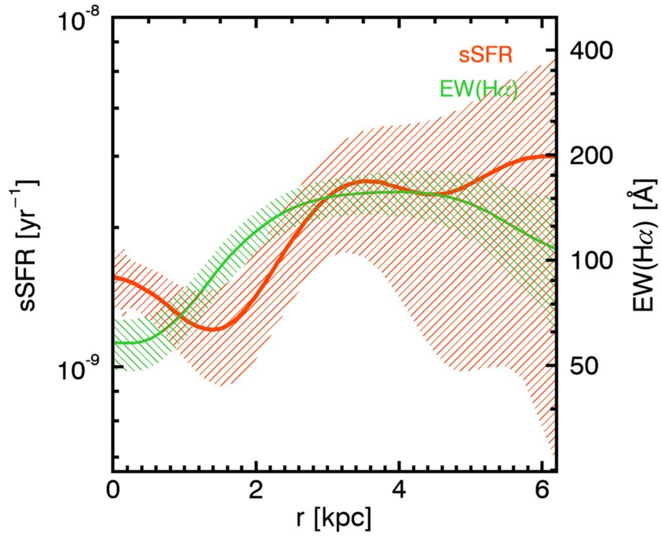

Figure 9. Here we show a comparison of the radial Hα equivalent (EW(Hα)) and specific star formation rate (sSFR) and profiles for GOODSN-18574. In green we plot the EW(Hα) that reflects the quotient of the Hα and surrounding continuum emission, which is often taken as a proxy for sSFR. In red we plot the sSFR that is the quotient of the SFR traced by the rest-500 μm continuum emission and the stellar mass. The sSFR is somewhat higher at large radii than in the center, suggesting that the stellar mass is growing more rapidly in the outskirts; the galaxy is building inside-out. The radial behavior of the EW(Hα) is fairly similar to the dust-corrected sSFR in this galaxy, meaning that in this galaxy, EW(Hα) is a good tracer of the sSFR.

find that inside $r < 5$ kpc, the two are similar. This similarity suggests that in this galaxy, EW(Hα) is an effective tracer of sSFR and can be used to determine where a galaxy is growing. We find that the sSFR increases radially, meaning that the galaxy is growing faster in the outskirts than in the center. This positive sSFR gradient is consistent with the idea that star formation, even after correcting for dust attenuation, is more extended than the existing stellar mass. The star formation makes the galaxy larger, growing it from the inside out.

3.4. Dust-corrected Hα and UV

Although EW(Hα) is a reasonably good proxy for sSFR, without accounting for dust, the radial distributions of star formation inferred from the different tracers—UV, Hα, and rest-500 μm—are clearly very different. We test this using a map of dust attenuation from spatially resolved SED modeling to correct the Hα and UV emission for the effects of dust. The SED modeling includes four bands that cover the rest-NUV-FUV: ACS/F606W and F435W, and UVIS/F336W and F275W, which we use to model a map of the UV continuum slope β (where $f_\lambda \propto \lambda^\beta$). We estimate the UV dust attenuation from β with

$$A_{1600\,\text{Å}} = 4.43 + 1.99\beta$$

(Meurer et al. 1999). We compute the attenuation at the wavelengths of our observations (A(Hα = 6563 Å) and A(UV = 1920 Å)) based on the Calzetti et al. (2000) attenuation law. These maps of $A_{\mathrm{H}\alpha}$ and A_{UV} are then used to correct the Hα- and UV-based maps of star formation (Figure 2) for the effects of dust (SFR(dustcorr) = SFR $\times$ $10^{0.4A}$). We quantify the efficacy of this dust correction by deriving sizes, concentrations, and radial profiles of the dust-corrected Hα- and UV-based star formation maps as described in the previous three subsections. Error bars comprise the formal error on the SPS fit of the β slope and the noise in the image.

Before dust correction, we measure sizes of r_e(Hα) = 4.8 $\pm$ 0.2 kpc and r_e(UV) = 6.2 $\pm$ 0.2 kpc, while after dust correction, we find r_e(Hα) = 3.9 $\pm$ 0.2 kpc and r_e(UV) = 3.8 $\pm$ 0.2 kpc. These are larger than although consistent within the large error bar on the rest-500 μm size of r_e(rest-500 μm) = 3.4 $\pm$ 0.7 kpc. Analogously, before dust correction, we find C(Hα) = 0.12 $\pm$ 0.01 and C(UV) = 0.04 $\pm$ 0.02, while after the correction, we find C(Hα) = 0.18 $\pm$ 0.02 and C(UV) = 0.16 $\pm$ 0.03. These values are somewhat lower than the concentration of the rest-500 μm emission, C(rest-500 μm) = 0.24 $\pm$ 0.03, but much closer than before the correction. These trends can be seen clearly in the dust-corrected radial profiles shown in Figure 8. There is surprisingly good agreement between IR and the dust-corrected Hα and UV, especially considering how dramatic the differences were before the dust correction. The exception is the center, where there is more dust-obscured star formation than inferred by the dust-corrected Hα and UV. This difference could indicate that the dust geometry is more complex than the simple foreground screen assumed for the spatially resolved SED fitting: if the stars and dust are mixed and some regions have $\tau \gg 1$, the rest-optical/UV colors may fail to recover the total quantity of dust-obscured star formation. The information gleaned from this exercise is that in this galaxy, the Hα and UV maps of star formation are significantly improved through attenuation maps from spatially resolved SED fitting to correct for dust, although some star formation may still be missed in the center.

4. Discussion

4.1. Evolution in Central Surface Density

To understand how the observed star formation contributes to structural evolution, we determine to which extent the star formation can account for the structural evolution we expect based on known population-wide scaling relations. First we investigate the evolution of the central stellar mass density of this galaxy that is due to dust-obscured star formation. Specifically, we determine to which extent the growth of the central stellar mass density can be accounted for by star formation. To do this, we use the central stellar mass surface density

$$\Sigma_{\rm cen} = M_{\rm cen}/r_{\rm cen}^2,$$

where $M_{\rm cen}$ is the mass contained in a central aperture with radius $r_{\rm cen}$. The relation between this central stellar mass surface density and the total stellar mass of galaxies $\Sigma_{\rm cen}$–M_* has a nearly constant slope of 0.86-0.89 over the redshift range $0.5 < z < 3$ (Barro et al. 2017). This relation results from the combined effect of the M_*–r_e and M_*–$n_{\rm sersic}$ relations and encapsulates the trend of increasing bulge dominance with increasing stellar mass. The key question is whether the star formation we observe is consistent with bulge building, moving the galaxy along this relation.

To answer this question, we compute the trajectory of GOODSN-18574 in the $\Sigma_{\rm cen}$–M_* plane due to star formation. If star formation can account for bulge growth, this trajectory should move the galaxy along the observed $\Sigma_{\rm cen}$–M_* relation (i.e., with the same slope found by Barro et al. 2017). Investigating this question requires at least a first-order correction for the PSF/beam the images. To estimate a correction for the PSF/beam, we use Sérsic models as described in Szomoru et al. (2010). Briefly, we use GALFIT best-fit parameters to produce a model for the galaxy that is not convolved with the PSF/beam. We then add the Sérsic model residuals back to this unconvolved model to produce an image that has a first-order correction for the PSF. The fits for the *HST* data are stable and trace the data well. The fit for the NOEMA data is not stable, with different initial conditions producing different fits. With the instability of this fit, we tested a large range of fit parameters and found that as long as the central aperture we used was larger than the beam, the measurement was robust against varied fitting parameters. Hence, instead of the 1 kpc aperture (Σ_1) used by Barro et al. (2017), we use a 2 kpc aperture and call this value $\Sigma_{\rm cen}$. Our error bar on this measurement includes the full range of beam corrections derived in the fitting.

In Figure 10 we show a comparison between the population Σ_1-M_* relation found by Barro et al. (2017; blue line), and the trajectory of GOODSN-18574 moves in this plane due to the star formation we observe (orange arrow). The population of star-forming galaxies at $1.0 < z < 1.4$ has $\Delta\Sigma_1/\Delta M_* = 0.88 \pm 0.03$ (Barro et al. 2017, Table 1). In GOODSN-18574 we find $\Delta\Sigma_{cen}/\Delta M_* = 0.9 \pm 0.2$. Thus we find that the star formation that builds this galaxy moves it along the Σ_1–M_* relation, suggesting that as star formation adds mass to this galaxy, we are witnessing the growth of its bulge. To the best of our information, star formation in this galaxy can build a bulge that is consistent with the structural relation of star-forming galaxies at this epoch.

4.2. Evolution in Size

We also compare the size growth of GOODSN-18574 that is due to star formation to the size growth of Andromeda progenitors that was empirically derived by Papovich et al.

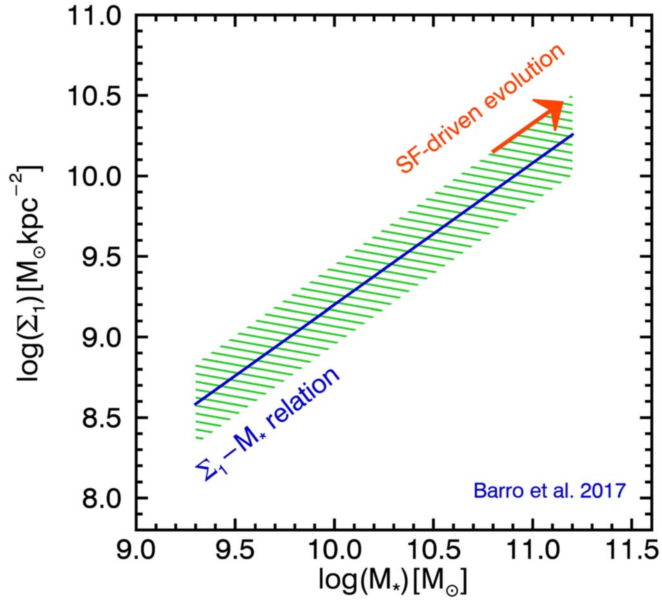

Figure 10. Σ_1–M_* relation for star-forming galaxies measured by Barro et al. (2017) ($\Delta\Sigma_1/\Delta M_* = 0.88 \pm 0.03$), shown by the blue line. The observed scatter in the relation $\sigma(\log\Sigma_1) \sim 0.25$ dex is shown by the green hatched region. The growth trajectory in this plane implied by our observations of GOODSN-18574 is $\Delta\Sigma_{\rm cen}/\Delta M_* = 0.9 \pm 0.2$, as shown by the orange arrow. Thus we find that the build-up of central stellar mass density implied by the dust-obscured star formation we measure in GOODSN-18574 moves it along the Σ_1–M_* relation, suggesting that as star formation adds mass to this galaxy, we witness the growth of its bulge.

(2015) using abundance matching. The average size growth of the population of the Andromeda progenitors based on a linear fit to the Papovich et al. (2015) size measurements is $\Delta r_e/\Delta M_* \sim 0.3$. This growth rate is consistent with star-forming galaxies in general (van Dokkum et al. 2015). We compare this average size-growth rate of Andromeda progenitors to that implied by the dust-obscured star formation we observe in GOODSN-18574. To estimate the implied size evolution ($\Delta r_e/\Delta M_*$) that is due to dust-obscured star formation in GOODSN-18574, we scale the best-fit model for the rest-500 μm emission to a ΔM_* and add it to the PSF-corrected profile of the existing stellar mass (see above). We choose $\Delta M_*/M_* \sim 10\%$ such that the instantaneous distribution of star formation at the start of the interval remains a reasonable assumption. Four our uncertainties we include estimates using Sérsic indices $n = 0.3$–3. Thus, we sum the radial profiles M_* (r) and ΔM_* (r) and measure the effective radius of the resulting radial profile using a growth curve.

The size growth implied by the star formation in GOODSN-18574 is $\Delta r_e/\Delta M_* = 0.3 \pm 0.1$. In this galaxy at this time, the expected size growth trajectory can in principle be explained simply by the addition of stellar mass that is due to star formation (without the need to invoke other processes such as merging to redistribute angular momentum after the stars are formed). This is shown in Figure 11: the size evolution of the population of Andromeda progenitors is shown by the points and blue line; our inferred growth trajectory based on dust-obscured star formation in GOODSN-18574 is shown as the orange arrow. Note, however, that the uncertainty on our rest-500 μm size measurement is still large, and including the full range of possibilities in this analysis means that $\Delta r_e/\Delta M_*$ can formally range from slightly negative to ~0.5. We

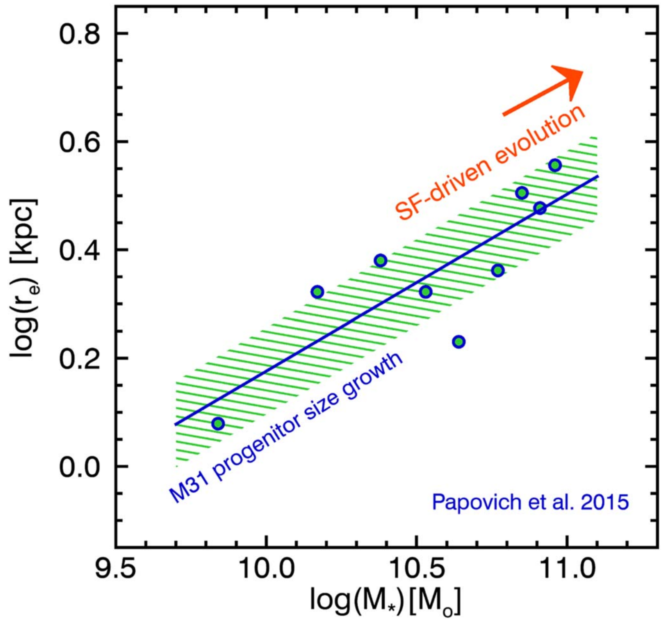

Figure 11. Size evolution of M31 progenitors empirically derived from abundance matching, shown by points (Papovich et al. 2015). The blue line shows the best fit, and the green hatched region shows the 1σ deviation of the points from the fit. The size growth implied by the dust-obscured star formation measured in GOODSN-18574 is shown by the orange arrow. The size growth implied by the dust-obscured star formation is consistent with the size evolution of M31 progenitors. This means that the expected size-growth trajectory can be explained simply by the addition of stellar mass that is due to star formation (see Section 4.2 for details).

therefore caution against interpreting this aspect of our analysis too strongly.

4.3. Comparison to Elliptical Progenitors

In addition to placing the dust-obscured star formation in GOODSN-18574 in the context of structural growth, we also compare it to other dust-continuum size measurements at intermediate redshift. In particular, we consider the growth patterns in this Andromeda progenitor at $z \sim 1$ compared to those in massive elliptical progenitors at $z \sim 2$. We compare to Tadaki et al. (2017), who present size measurements for Hα-selected galaxies with $M_* > 10^{11}$ at $z = 2.19$ and $z = 2.53$. No lower mass galaxies were detected with sufficient fidelity to measure a size, hence there are no size measurements for galaxies with $M_* < 10^{11}$. Barro et al. (2016) also studied dust continuum sizes in massive galaxies at $z \sim 2$. However, we do not include them here as they were specifically selected to be compact in optical light, which complicates the comparison.

First, we compare rest-optical and dust continuum sizes. To probe similar rest-optical wavelengths, we use H_{F160W} sizes for the massive comparison sample of galaxies at $z \sim 2$ and the J_{F125W} size for GOODSN-18574 at $z = 1.25$, corresponding to rest wavelengths of ~5000 Å and 5900 Å, respectively (van der Wel et al. 2014, from CANDELS). As shown in the left panel of Figure 13, in all galaxies, the dust continuum is more compact than the rest-optical. This means that all galaxies studied here display significant dust gradients and likely dust attenuation gradients, although the latter depend on the geometry of the dust. In GOODSN-18574, the submm size is more compact than the optical size by a factor of $r_e(\text{optical})/r_e(\text{submm}) = 1.4$; in the massive $z \sim 2$ comparison

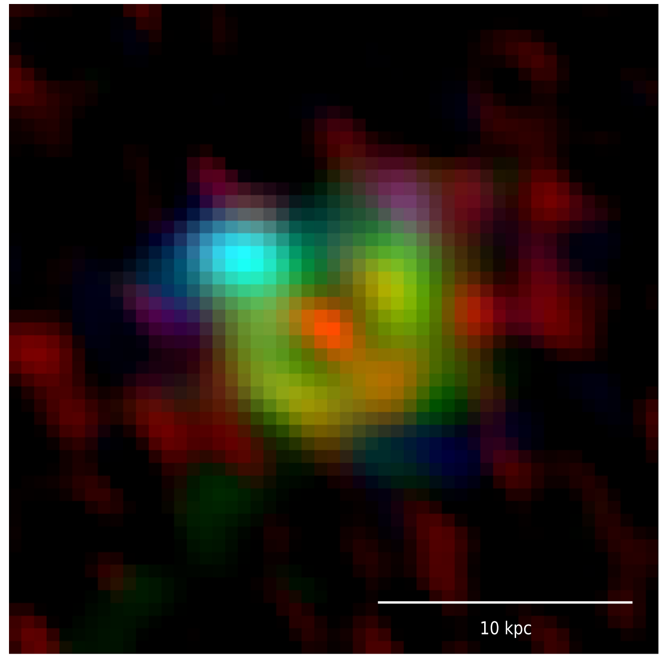

Figure 12. Three-color image of star formation with UV in blue, Hα in green, and rest-500 μm in red. The three different tracers trace distinctly different regions of the galaxy.

sample, it is on average a factor of 2 ($r_e(\text{optical})/r_e(\text{submm}) = 2.0$). Relative to the rest-optical, the dust continuum in GOODSN-18574 is less dramatically compact than in the massive elliptical progenitors; it is similar to the galaxies of Tadaki et al. (2017) with the most extended dust continuum emission. Studies of SMGs at $z \sim 2.5$ also find compact 870 μm emission, with average effective radii 2–4 times more compact in the submm than in the rest-frame optical (e.g., Simpson et al. 2015, 2017; Hodge et al. 2016). Similarly to the mass-selected sample of Tadaki et al. (2017), the submm flux-selected samples of SMGs are likely progenitors of local massive early-type galaxies (e.g., Tacconi et al. 2008; Toft et al. 2014; Ikarashi et al. 2015; Hodge et al. 2016; Simpson et al. 2017).

Second, we compare the rest-optical and stellar mass sizes. While the dust continuum is nearly always more compact than the rest-optical emission, if these galaxies have color gradients, they will also have M/L gradients. Figure 13 shows $r_e(M_*)$ versus $r_e(\text{light})$ for the full population of galaxies as computed in Lang et al. (2014). This shows that the effective radius is almost always smaller in mass than in light: the stellar mass is nearly always more compact than the rest-optical light.

Finally, we compare the dust continuum and stellar mass sizes. The top right panel of Figure 13 shows $r_e(\text{submm})$ versus $r_e(M_*)$ for all galaxies for which we have a measurement of the stellar mass effective radius. GOODSN-18574 has $r_e(\text{submm}) \gtrsim r_e(M_*)$, as do three of the seven galaxies in the sample of Tadaki et al. (2017), while the remaining four out of seven of galaxies in this sample have $re(\text{submm}) < r_e(M_*)$. At face value, this means that there is a mix of dust continuum sizes ranging from smaller to slightly larger than the stellar mass sizes. If we were to take the submm emission as a proxy for star formation, $r_e(\text{submm}) < r_e(M_*)$, this might be explained by galaxies undergoing a compaction event in which their dense central regions are grown by a dissipative event that brings gas to the center and that induces central star formation

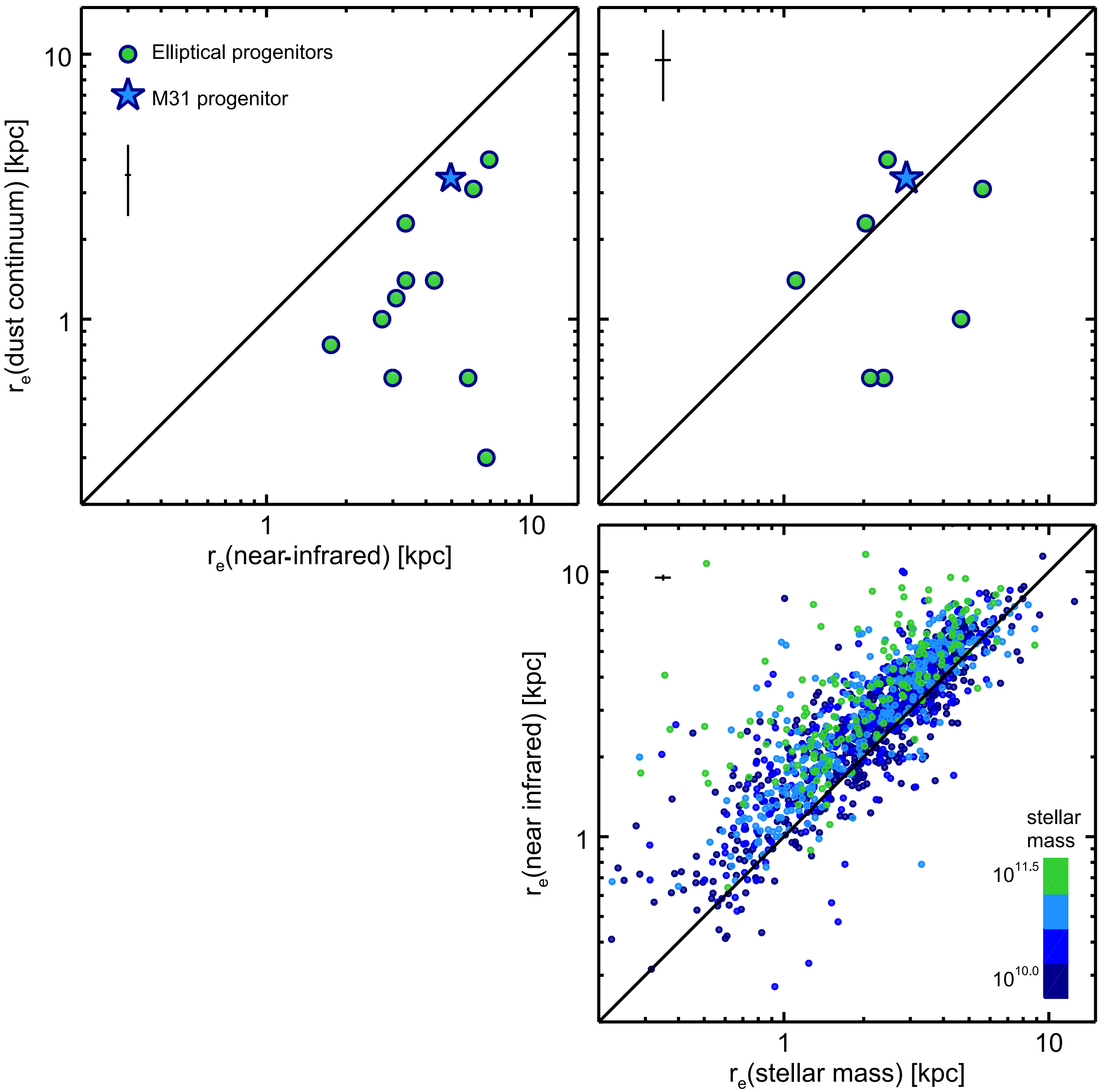

Figure 13. Size comparison of the M31 progenitor GOODSN-18574 ($M_* = 6.76 \times 10^{10}\, M_\odot$ at $z = 1.25$) and the massive elliptical galaxy progenitors of Tadaki et al. (2017; $M_* > 1 \times 10^{11}\, M_\odot$ at $z = [2.19, 2.53]$). The left panel shows that in all the galaxies, the dust continuum is more compact than the near-infrared (rest-optical) continuum emission. The bottom right panel shows that in most galaxies with $M > 1.6 \times 10^{10}$ at $1 < z < 2.5$, the stellar mass is more compact than the near-infrared continuum emission. The top right panel shows that in roughly half the galaxies, in these studies the submm is more compact than the stellar mass and in the other half, it is more extended. Taken at face value, this would suggest that half the galaxies become more compact as a result of star formation, and the other half retain the same size or grow slightly larger. However, the very high central dust column densities may cause an underestimation of the central stellar mass densities. This would mean that the stellar mass sizes are in fact smaller than plotted here, which would move the points to the left. Note that four galaxies are not present here because we did not conduct spatially resolved mass modeling for galaxies with $H_{F160W} > 23.5$ (see Wuyts et al. 2012; Lang et al. 2014). The crosses in the upper left corner of each plot show the measurement uncertainty. For the near-infrared and dust continuum radii, this is the average uncertainty from van der Wel et al. (2014) and Tadaki et al. (2017), respectively. For the stellar mass, this is the fit uncertainty measured for GOODSN-18574. However, with high dust column densities, the systematic uncertainty on the stellar mass sizes is larger.

(e.g., Dekel & Burkert 2014; Zolotov et al. 2015). On the other hand, $r_e(\mathrm{submm}) > r_e(M_*)$ most simply implies that at the time of observation, the galaxy is building inside out, with star formation increasing the effective radius (e.g., Nelson et al. 2012; van Dokkum et al. 2015). Statistics cannot be drawn from one galaxy, but that GOODSN-18574 does not show evidence for compaction while a number of galaxies in the Tadaki et al. (2017) sample do might reflect the theoretical argument that compaction is more common in high-mass galaxies at high redshift when gas surface densities were higher.

One important note here is that given the high dust columns toward the centers of the massive $z \sim 2$ galaxies that are implied by the submm data, the expected dust attenuation is very high. Interpreting the submm data as a tracer of molecular gas and using the molecular gas column density to infer dust attenuation (as in Section 2.5), at ~6000 Å, we infer $\tau \sim 5$ in the central ~kpc of the $z \sim 2$ galaxies and $\tau \sim 2.5$ in the central ~kpc of GOODSN-18574. With central $\tau \gg 1$ even at rest-frame wavelengths of ~6000 Å, the stellar mass maps may be missing stars. Consequently, the central stellar mass surface density inferred based on rest-UV/optical data may be too low, meaning that the stellar mass effective radii may also be smaller than measured. If this were in fact the case, the effect in the top right panel of Figure 13 would be that points would be shifted to the left: a higher fraction of galaxies may in reality have $r_e(\text{submm}) > r_e(M_*)$ and be growing inside out.

5. Summary

In this paper we investigated dust-obscured bulge growth in an Andromeda progenitor at $z = 1.25$. We combined new mm dust continuum mapping from the NOEMA interferometer with Hα, UV, and stellar mass maps to place constraints on the formation pathways for bulge-disk systems.

GOODSN-18574 displays a ring in Hα and UV emission, which implies that the central star formation is strongly centrally suppressed in an absolute sense. However, when imaged at mm wavelengths, we instead see centrally concentrated dust-continuum emission, meaning that this ring of unobscured star formation is likely filled in by dust-obscured star formation. This suggests that in this galaxy, the ring observed in Hα and UV emission is caused by dust-obscuration rather than centrally suppressed star formation. This is the main result of this paper: the bulge of this galaxy is building by dust-obscured star formation.

To quantify this bulge building, we determined which fraction of the bulge growth that is underway at $z \sim 1$ can be accounted for by the star formation we observe. In Section 4.1 we derived the quantity of bulge growth relative to disk growth that would be required in order for a galaxy to remain on the scaling relation between central stellar mass surface density (as a proxy for bulge mass) and total stellar mass. We find that the dust-obscured star formation we observe would move this galaxy along a trajectory with the same slope as this relation. Within the (significant) errors on this measurement, in this galaxy at this epoch, bulge growth can be explained by dust-obscured star formation. This galaxy lies above the main sequence, and its optical morphology might suggest that it is undergoing a minor merger and/or has a large clump in the disk. Taken together, our observations are consistent with a picture in which merging and disk instabilities drive gas to the center of the galaxy, boosting the global star formation rate. This then moves the galaxy above the main sequence and builds the bulge. This could be seen in a framework in which galaxies oscillate around the star-forming main sequence as a result of variations in accretion rate (including mergers as "clumpy accretion"; e.g., Forbes et al. 2012, 2014; Nelson et al. 2016b; Tacchella et al. 2016b, 2016a, 2018; Orr et al. 2017; Sparre et al. 2017).

The bulge and disk of this galaxy are building simultaneously. Although the bulge growth is largely dust obscured, the disk growth is apparent in the rest-500 μm, Hα, and UV. Furthermore, while the dust-obscured star formation is more concentrated than the un-obscured star formation, it has a similar or larger size than the stellar mass. The star formation we observe, although the errors are large, is consistent with the expected size evolution of Andromeda progenitors at this epoch: it gradually increases at a rate of $\Delta r_e/\Delta M_* \sim 0.3$.

This is in contrast to the dust continuum measurements of some massive galaxies at $z \sim 2$, which are the putative progenitors of local massive elliptical galaxies. While mm/submm observations reveal dust-obscured bulge/dense core growth for both Andromeda and massive elliptical progenitors, some of the very massive galaxies at $z \sim 2$ may become more compact as a result of star formation. It is expected that this strong form of compaction is more common at $z = 2$ than $z = 1$ because gas fractions and merger rates are higher there. However, given the extremely high dust column densities toward the centers of these galaxies, we may be significantly underestimating the central stellar mass surface density that is already present. If this were the case, these galaxies would not in fact be undergoing compaction in the sense of physically shrinking in radius. Spatially resolved stellar population synthesis modeling that takes into account resolved mm constraints is needed before this can be conclusively answered.

The ability to map the structural growth of galaxies provides powerful constraints on the physical drivers of their evolution. This requires maps of star formation and stellar mass that account for the effects of dust and age. In this paper we showed that dust-obscured star formation can play a key role in our understanding of the structural evolution of galaxies. To reliably determine how galaxies are growing, and whether dust-obscured star formation is responsible for the building of bulges and dense cores, dust continuum mapping with high spatial resolution statistical samples of galaxies at a range of redshifts beyond $z > 1$ and across the SFR–M_* plane is required. Because the progenitors of galaxies such as the Milky Way and Andromeda have lower masses and correspondingly lower gas masses and metallicities, longer integration times will be needed to map them—but these measurements are key to understanding how bulges build. Additionally, high-resolution mapping of molecular gas kinematics will be essential to placing more stringent constraints on the physical processes that are responsible for building the dense centers of galaxies.

The authors thank the anonymous referee, whose comments improved this manuscript. We are grateful to Melanie Krips, Karl Schuster, and all the staff of the IRAM facilities for their excellent support.

ORCID iDs

Erica J. Nelson https://orcid.org/0000-0002-7524-374X
Ken-ichi Tadaki https://orcid.org/0000-0001-9728-8909
Linda J. Tacconi https://orcid.org/0000-0002-1485-9401
Dieter Lutz https://orcid.org/0000-0003-0291-9582
Natascha M. Förster Schreiber https://orcid.org/0000-0003-4264-3381
Anna Cibinel https://orcid.org/0000-0003-4578-514X
Stijn Wuyts https://orcid.org/0000-0003-3735-1931
Philipp Lang https://orcid.org/0000-0002-5681-3575
Joel Leja https://orcid.org/0000-0001-6755-1315
Pascal A. Oesch https://orcid.org/0000-0001-5851-6649
Sirio Belli https://orcid.org/0000-0002-5615-6018
Rebecca L. Davies https://orcid.org/0000-0002-3324-4824

Reinhard Genzel https://orcid.org/0000-0002-2767-9653
Sedona H. Price https://orcid.org/0000-0002-0108-4176
Hannah Übler https://orcid.org/0000-0003-4891-0794

References

Abraham, R. G., Tanvir, N. R., Santiago, B. X., et al. 1996, MNRAS, 279, L47
Abraham, R. G., Valdes, F., Yee, H. K. C., & van den Bergh, S. 1994, ApJ, 432, 75
Arnouts, S., Cristiani, S., Moscardini, L., et al. 1999, MNRAS, 310, 540
Ashby, M. L. N., Willner, S. P., Fazio, G. G., et al. 2013, ApJ, 769, 80
Barger, A. J., Cowie, L. L., Sanders, D. B., et al. 1998, Natur, 394, 248
Barro, G., Faber, S. M., Koo, D. C., et al. 2017, ApJ, 840, 47
Barro, G., Kriek, M., Pérez-González, P. G., et al. 2016, ApJL, 827, L32
Behroozi, P. S., Wechsler, R. H., & Conroy, C. 2013, ApJ, 770, 57
Bendo, G. J., Baes, M., Bianchi, S., et al. 2015, MNRAS, 448, 135
Bendo, G. J., Boselli, A., Dariush, A., et al. 2012, MNRAS, 419, 1833
Bendo, G. J., Wilson, C. D., Pohlen, M., et al. 2010, A&A, 518, L65
Blain, A. W., Smail, I., Ivison, R. J., Kneib, J.-P., & Frayer, D. T. 2002, PhR, 369, 111
Bland-Hawthorn, J., & Gerhard, O. 2016, ARA&A, 54, 529
Bournaud, F. 2016, in Galactic Bulges, ed. E. Laurikainen, R. Peletier, & D. Gadotti, Vol. 418 (Berlin: Springer), 355
Brammer, G. B., van Dokkum, P. G., Franx, M., et al. 2012, ApJS, 200, 13
Bruzual, G., & Charlot, S. 2003, MNRAS, 344, 1000
Calzetti, D., Armus, L., Bohlin, R. C., et al. 2000, ApJ, 533, 682
Casey, C. M. 2012, MNRAS, 425, 3094
Chabrier, G. 2003, PASP, 115, 763
Cibinel, A., Le Floc'h, E., Perret, V., et al. 2015, ApJ, 805, 181
Conroy, C., & Wechsler, R. H. 2009, ApJ, 696, 620
Coppin, K., Halpern, M., Scott, D., et al. 2008, MNRAS, 384, 1597
Courteau, S., Widrow, L. M., McDonald, M., et al. 2011, ApJ, 739, 20
Dekel, A., & Burkert, A. 2014, MNRAS, 438, 1870
Dekel, A., Sari, R., & Ceverino, D. 2009, ApJ, 703, 785
Dickinson, M., Giavalisco, M. & GOODS Team 2003, in The Mass of Galaxies at Low and High Redshift, ed. R. Bender & A. Renzini (Berlin: Springer), 324
Dorman, C. E., Guhathakurta, P., Fardal, M. A., et al. 2012, ApJ, 752, 147
Elbaz, D., Dickinson, M., Hwang, H. S., et al. 2011, A&A, 533, A119
Engelbracht, C. W., Hunt, L. K., Skibba, R. A., et al. 2010, A&A, 518, L56
Epinat, B., Contini, T., Le Fèvre, O., et al. 2009, A&A, 504, 789
Forbes, J., Krumholz, M., & Burkert, A. 2012, ApJ, 754, 48
Forbes, J. C., Krumholz, M. R., Burkert, A., & Dekel, A. 2014, MNRAS, 438, 1552
Förster Schreiber, N. M., Genzel, R., Bouché, N., et al. 2009, ApJ, 706, 1364
Förster Schreiber, N. M., Genzel, R., Lehnert, M. D., et al. 2006, ApJ, 645, 1062
Galametz, M., Kennicutt, R. C., Albrecht, M., et al. 2012, MNRAS, 425, 763
Geehan, J. J., Fardal, M. A., Babul, A., & Guhathakurta, P. 2006, MNRAS, 366, 996
Genzel, R., Burkert, A., Bouché, N., et al. 2008, ApJ, 687, 59
Genzel, R., Tacconi, L. J., Eisenhauer, F., et al. 2006, Natur, 442, 786
Genzel, R., Tacconi, L. J., Kurk, J., et al. 2013, ApJ, 773, 68
Giavalisco, M., Ferguson, H. C., Koekemoer, A. M., et al. 2004, ApJL, 600, L93
Grogin, N. A., Kocevski, D. D., Faber, S. M., et al. 2011, ApJS, 197, 35
Hayward, C. C., Kereš, D., Jonsson, P., et al. 2011, ApJ, 743, 159
Hodge, J. A., Carilli, C. L., Walter, F., et al. 2012, ApJ, 760, 11
Hodge, J. A., Swinbank, A. M., Simpson, J. M., et al. 2016, ApJ, 833, 103
Hunt, L. K., Draine, B. T., Bianchi, S., et al. 2015, A&A, 576, A33
Ikarashi, S., Ivison, R. J., Caputi, K. I., et al. 2015, ApJ, 810, 133
Ilbert, O., Arnouts, S., McCracken, H. J., et al. 2006, A&A, 457, 841
Immeli, A., Samland, M., Westera, P., & Gerhard, O. 2004, ApJ, 611, 20
Kassin, S. A., Weiner, B. J., Faber, S. M., et al. 2007, ApJL, 660, L35
Kassin, S. A., Weiner, B. J., Faber, S. M., et al. 2012, ApJ, 758, 106
Kennicutt, R. C., Jr. 1998, ARA&A, 36, 189
Koekemoer, A. M., Faber, S. M., Ferguson, H. C., et al. 2011, ApJS, 197, 36
Kormendy, J. 2016, in Galactic Bulges, ed. E. Laurikainen, R. Peletier, & D. Gadotti, Vol. 418 (Berlin: Springer), 431
Krist, J. 1995, in ASP Conf. Ser.77, Astronomical Data Analysis Software and Systems IV, ed. R. A. Shaw, H. E. Payne, & J. J. E. Hayes (San Francisco, CA: ASP), 349
Lang, P., Wuyts, S., Somerville, R. S., et al. 2014, ApJ, 788, 11
Law, D. R., Steidel, C. C., Erb, D. K., et al. 2009, ApJ, 697, 2057
Leja, J., Johnson, B., Conroy, C., et al. 2018, ApJ, submitted (arXiv:1812.05608)
Leja, J., Johnson, B. D., Conroy, C., Dokkum, P. G. v., & Byler, N. 2017, ApJ, 837, 170
Leja, J., van Dokkum, P. G., Momcheva, I., et al. 2013, ApJL, 778, L24
Lilly, S. J., & Carollo, C. M. 2016, ApJ, 833, 1
Liu, F. S., Jiang, D., Faber, S. M., et al. 2017, ApJL, 844, L2
Liu, F. S., Jiang, D., Guo, Y., et al. 2016, ApJL, 822, L25
Lonsdale Persson, C. J., & Helou, G. 1987, ApJ, 314, 513
Lotz, J. M., Primack, J., & Madau, P. 2004, AJ, 128, 163
Lutz, D., Poglitsch, A., Altieri, B., et al. 2011, A&A, 532, A90
Madau, P., & Dickinson, M. 2014, ARA&A, 52, 415
Magnelli, B., Popesso, P., Berta, S., et al. 2013, A&A, 553, A132
Menéndez-Delmestre, K., Blain, A. W., Smail, I., et al. 2009, ApJ, 699, 667
Meurer, G. R., Heckman, T. M., & Calzetti, D. 1999, ApJ, 521, 64
Momcheva, I. G., Brammer, G. B., van Dokkum, P. G., et al. 2016, ApJS, 225, 27
Montalto, M., Seitz, S., Riffeser, A., et al. 2009, A&A, 507, 283
Moster, B. P., Naab, T., & White, S. D. M. 2013, MNRAS, 428, 3121
Murphy, E. J., Momjian, E., Condon, J. J., et al. 2017, ApJ, 839, 35
Nelson, E. J., van Dokkum, P. G., Brammer, G., et al. 2012, ApJL, 747, L28
Nelson, E. J., van Dokkum, P. G., Förster Schreiber, N. M., et al. 2016b, ApJ, 828, 27
Nelson, E. J., van Dokkum, P. G., Momcheva, I., et al. 2013, ApJL, 763, L16
Nelson, E. J., van Dokkum, P. G., Momcheva, I. G., et al. 2016a, ApJL, 817, L9
Newman, S. F., Genzel, R., Förster Schreiber, N. M., et al. 2013, ApJ, 767, 104
Oesch, P., Montes, M., Reddy, N., et al. 2018, ApJS, 237, 12
Orr, M. E., Hayward, C. C., Nelson, E. J., et al. 2017, ApJL, 849, L2
Papovich, C., Labbé, I., Quadri, R., et al. 2015, ApJ, 803, 26
Peng, C. Y., Ho, L. C., Impey, C. D., & Rix, H.-W. 2002, AJ, 124, 266
Pohlen, M., Cortese, L., Smith, M. W. L., et al. 2010, A&A, 518, L72
Pope, A., Chary, R.-R., Alexander, D. M., et al. 2008, ApJ, 675, 1171
Reddy, N. A., Erb, D. K., Pettini, M., Steidel, C. C., & Shapley, A. E. 2010, ApJ, 712, 1070
Reddy, N. A., Oesch, P. A., Bouwens, R. J., et al. 2017, arXiv:1705.09302
Reddy, N. A., Steidel, C. C., Fadda, D., et al. 2006, ApJ, 644, 792
Saglia, R. P., Fabricius, M., Bender, R., et al. 2010, A&A, 509, A61
Salpeter, E. E. 1955, ApJ, 121, 161
Scoville, N., Aussel, H., Sheth, K., et al. 2014, ApJ, 783, 84
Scoville, N., Sheth, K., Aussel, H., et al. 2016, ApJ, 820, 83
Sérsic, J. L. 1968, in Atlas de Galaxias Australes, ed. J. L. Sersic (Cordoba: Observatorio Astronomico)
Simpson, J. M., Smail, I., Swinbank, A. M., et al. 2015, ApJ, 799, 81
Simpson, J. M., Smail, I., Swinbank, A. M., et al. 2017, ApJ, 839, 58
Skelton, R. E., Whitaker, K. E., Momcheva, I. G., et al. 2014, ApJS, 214, 24
Smith, M. W. L., Eales, S. A., Gomez, H. L., et al. 2012, ApJ, 756, 40
Sparre, M., Hayward, C. C., Feldmann, R., et al. 2017, MNRAS, 466, 88
Stott, J. P., Swinbank, A. M., Johnson, H. L., et al. 2016, MNRAS, 457, 1888
Szomoru, D., Franx, M., van Dokkum, P. G., et al. 2010, ApJL, 714, L244
Tacchella, S., Carollo, C. M., Förster Schreiber, N. M., et al. 2018, ApJ, 859, 56
Tacchella, S., Dekel, A., Carollo, C. M., et al. 2016a, MNRAS, 458, 242
Tacchella, S., Dekel, A., Carollo, C. M., et al. 2016b, MNRAS, 457, 2790
Tacconi, L. J., Genzel, R., Neri, R., et al. 2010, Natur, 463, 781
Tacconi, L. J., Genzel, R., Smail, I., et al. 2008, ApJ, 680, 246
Tacconi, L. J., Neri, R., Genzel, R., et al. 2013, ApJ, 768, 74
Tadaki, K.-i., Genzel, R., Kodama, T., et al. 2017, ApJ, 834, 135
Tamm, A., Tempel, E., Tenjes, P., Tihhonova, O., & Tuvikene, T. 2012, A&A, 546, A4
Toft, S., Smolčić, V., Magnelli, B., et al. 2014, ApJ, 782, 68
Torrey, P., Wellons, S., Ma, C.-P., Hopkins, P. F., & Vogelsberger, M. 2017, MNRAS, 467, 4872
Torrey, P., Wellons, S., Machado, F., et al. 2015, MNRAS, 454, 2770
van der Wel, A., Bell, E. F., Häussler, B., et al. 2012, ApJS, 203, 24
van der Wel, A., Franx, M., van Dokkum, P. G., et al. 2014, ApJ, 788, 28
van Dokkum, P. G., Brammer, G., Fumagalli, M., et al. 2011, ApJL, 743, L15
van Dokkum, P. G., Leja, J., Nelson, E. J., et al. 2013, ApJ, 771, L35
van Dokkum, P. G., Nelson, E. J., Franx, M., et al. 2015, ApJ, 813, 23
Walterbos, R. A. M., & Greenawalt, B. 1996, ApJ, 460, 696
Wang, W., Faber, S. M., Liu, F. S., et al. 2017, MNRAS, 469, 4063
Wellons, S., & Torrey, P. 2017, MNRAS, 467, 3887
Whitaker, K. E., Franx, M., Leja, J., et al. 2014, ApJ, 795, 104

Whitaker, K. E., van Dokkum, P. G., Brammer, G., & Franx, M. 2012, ApJL, 754, L29
Wisnioski, E., Förster Schreiber, N. M., Wuyts, S., et al. 2015, ApJ, 799, 209
Wisnioski, E., Glazebrook, K., Blake, C., et al. 2011, MNRAS, 417, 2601
Wuyts, E., Kurk, J., Förster Schreiber, N. M., et al. 2014, ApJL, 789, L40
Wuyts, E., Wisnioski, E., Fossati, M., et al. 2016, ApJ, 827, 74
Wuyts, S., Förster Schreiber, N. M., Genzel, R., et al. 2012, ApJ, 753, 114
Wuyts, S., Förster Schreiber, N. M., Lutz, D., et al. 2011, ApJ, 738, 106
Wuyts, S., Förster Schreiber, N. M., Nelson, E. J., et al. 2013, ApJ, 779, 135
Zibetti, S., Charlot, S., & Rix, H.-W. 2009, MNRAS, 400, 1181
Zolotov, A., Dekel, A., Mandelker, N., et al. 2015, MNRAS, 450, 2327